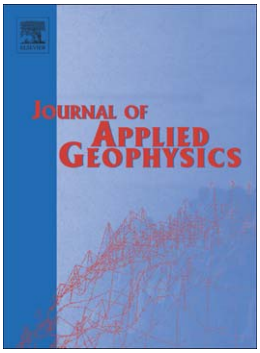

Combined three-dimensional electric and seismic tomography study on the Åknes rockslide in western Norway

Björn Heincke, Thomas Günther, Einar Dalsegg, Jan Steinar Rønning, Guri Venvik Ganerød, Harald Elvebakk

PII: S0926-9851(09)00158-X
DOI: doi: 10.1016/j.jappgeo.2009.12.004
Reference: APPGEO 1836

To appear in: *Journal of Applied Geophysics*

Received date: 29 April 2009
Accepted date: 15 December 2009

Please cite this article as: Heincke, Björn, Günther, Thomas, Dalsegg, Einar, Rønning, Jan Steinar, Ganerød, Guri Venvik, Elvebakk, Harald, Combined three-dimensional electric and seismic tomography study on the Åknes rockslide in western Norway, *Journal of Applied Geophysics* (2010), doi: 10.1016/j.jappgeo.2009.12.004

Combined three-dimensional electric and seismic tomography study on the Åknes rockslide in western Norway

Björn Heincke[*,a,d], Thomas Günther[b], Einar Dalsegg[a], Jan Steinar Rønning[a,c], Guri Venvik Ganerød[a], Harald Elvebakk[a]

[a] *Geological Survey of Norway (NGU), Leiv Eirikssons vei 39, 7491 Trondheim, Norway*
[b] *Leibniz Institute for Applied Geophysics, Stilleweg 2, 30655 Hannover, Germany*
[c] *Norwegian University of Science and Technology (NTNU), 7491 Trondheim, Norway*
[d] *Present address: IFM-GEOMAR, Wischhofstr. 1-3, 24148 Kiel, Germany*

Abstract

We present a combined 3-D geoelectric and seismic tomography study conducted on the large Åknes rockslide in western Norway. Movements on the slope are strongly influenced by water infiltration, such that the hydrogeological regime is considered as a critical factor affecting the slope stability. The aim of our combined geophysical study was to identify and visualize the main shallow tension fractures and to determine their effect on hydraulic processes by comparing the geophysical results with information from borehole logging and tracer tests. To resolve the complex subsurface conditions of the highly fractured rock mass, a three-dimensional set-up was chosen for our seismic survey. To map the water distribution within the rock mass, a pattern of nine intersecting 2-D geoelectric profiles covered the complete unstable slope. Six of them that crossed the seismic survey area were considered as a single data set in a 3-D inversion. For both methods, smoothing-constraint inversion algorithms were used, and the forward calculations and parameterizations were based on unstructured triangular meshes. A pair of parallel shallow low-velocity anomalies ($<$1400 m/s) observed in the final seismic tomogram was immediately underlain by two anomalies with resistivities $<$ 13 kΩm in the resistivity tomogram. In combination with borehole logging results, the low-velocity and resistivity anomalies could be associated with the drained and water-filled part of the tension fractures, respectively. There were indications from impeller flowmeter measurements and tracer tests that such tension fractures intersected several other water-filled fractures and were responsible for distinct changes of the main groundwater flow paths.

Key words: rockslides, 3-D seismic tomography, 3-D electrical resistivity tomography

1. Introduction

Rockslides are highly complex features and many factors such as fracture and fault distribution, ground water conditions, foliation and characteristics of sliding plane(s) can affect slope stabilities and movements. Data from aerial and remote-sensing techniques, geomorphological and geological mapping, geotechnical investigations and borehole logging can provide detailed information about most of the parameters affecting slope stabilities. However, all such information is gathered at or close to the surface or within boreholes. Because geophysical measurements allow both spatial and temporal variations of physical parameters in the subsurface to be studied in a non-invasive form, they can provide the missing information. Unfortunately, physical parameters obtained from geophysics are rarely linked in a simple manner to the required geological and mechanical properties on rockslides (Jongmans and Garambois, 2007). Several geophysical methods are, therefore, usually employed at the same location and linked with all other available data to reduce the number of potential geological models (see overview papers about geophysical investigations on unstable slopes by McCann and Foster (1990); Hack (2000); Jongmans and Garambois (2007)).

Two of the most commonly applied methods on rockslides are electrical resistivity tomography (e.g. Batayneh and Al-Diabat, 2002; Lebourg et al., 2005; Godio et al., 2006; Supper et al., 2007) and seismic P-wave refraction tomography (e.g. Jongmans et al., 2000; Havenith et al., 2002; Méric et al., 2005; Godio et al., 2006; Heincke et al., 2006). Electrical resistivity tomography can provide information about weathering and fracturing. Depending on water saturation conditions (Jongmans and Garambois, 2007), fracturing can lead both to an increase (Méric et al., 2005) or a decrease (Lebourg et al., 2005) in the resistivity relative to the undisturbed rock mass. In some studies, resistivity measurements allow individual water aquifers (e.g. Lebourg et al., 2005) or even the main rupture surfaces (Batayneh and

*Corresponding author
Tel.: +49 431 600-2556
Fax: +49 431 600-2915

Al-Diabat, 2002; Lebourg et al., 2005) to be determined, particularly if the lower part of the sliding mass has increased moisture content relative to the stable rock mass. Seismic refraction tomography usually provides information about the extent of slope instabilities, because P-wave velocity (v_p) is significantly decreased in fractured and weathered rock relative to intact rock (Jongmans et al., 2000; Méric et al., 2005; Jongmans and Garambois, 2007). Values as low as $v_p < 1500$ m/s have been determined from tomographic studies on rockslides in unsaturated conditions (Heincke et al., 2006). Strong velocity variations are often observed not only in vertical but also lateral directions (Méric et al., 2005; Heincke et al., 2006), suggesting alternation of nearly vertical fracture zones and intact rock. Individual fractures are generally not resolvable by this method, but principal directions of steeply-dipping fracture zones can usually be detected (Heincke et al., 2006). P-wave velocity models obtained from seismic tomography can also be used to improve results from reflection seismic and micro-seismic studies (Spillmann et al., 2007) on rockslides.

Limited accessibility and the large extent of many rockslides make 3-D surveys expensive and laborious such that usually only individual profiles or patterns of a few crossing 2-D profiles are collected. However, 2-D investigations are inherently limited to resolve simple two-dimensional subsurface conditions, which are not typical for highly disrupted rockslide bodies. Heincke et al. (2006) observed that the shallow fracture distribution on a complex rockslide in Switzerland could not be reconstructed from tomograms of intersecting seismic profiles, but it could be from a tomogram derived from a "true" three-dimensional seismic experiment at the same location. Results from geoelectric tomography are to a larger extent sensitive to variations away from the 2-D profiles and under favorable circumstances a 3-D inversion of a dense pattern of geoelectric profiles may provide reliable subsurface information about complex structures (Gharibi and Bentley, 2005).

We present here an integrated tomographic study of 3-D seismic refraction and electrical restivity data collected across the upper part of the large Åknes rockslide in western Norway. Because pore pressure variations and water distribution are important factors influencing the evolution of the rockslide (Frei, 2008), it is important to understand better the interaction of the hydraulic and kinematic processes. In this context, the geophysical investigations should

provide us with 3-D knowledge on the distribution of the main structures (e.g. fracture zones) and hydraulic features (e.g. primary water flow paths). In combination with other information from borehole logging and tracer tests, the effect of the structural setting on the water regime can then be investigated. For our 3-D geophysical experiment we chose the upper central part of the rockslide, because at this location the hydraulic regime is affected by large-scaled tension fractures in an unclear manner. A borehole in this region allow us to correlate results from the surface geophysics and borehole logging.

We first give an overview of the rockslide, including a description of the geology and results from other relevant investigations (section 2). Further we describe our geoelectrical and seismic experiments and employed algorithms in section 3. Results from both methods are interpreted together with information from borehole logging, tracer tests and surface observations in section 4. Since our seismic survey is restricted to the upper central part of the rockslide, our interpretation will focus on this relatively small region.

2. Åknes site

[Figure 1 about here.]

Location

The Åknes rockslide is located on the western flank of the Sunnylvsfjord in western Norway (see Fig. 1a) - an area distinguished by frequent rock slope failures over the past 10 000 years (Blikra et al., 2005). Failure of the Åknes rockslide would probably cause a large tsunami (Blikra et al., 2005) that poses a major threat to the villages Stranda and Hellesylt and the tourist resort Geiranger along the shorelines of the narrow Sunnylvsfjord and Geirangerfjord (Fig. 1a). To prevent such destructive events, the Åknes/Tafjord project was initiated in 2004 with the aim of building up a reliable early-warning system (Blikra, 2008). In the framework of this project, research aspects are aimed at improving our understanding of the internal processes of such complex rockslides. Investigations comprise geological mapping, multi-tracer tests, geophysical surveys, a micro-seismic network, borehole logging, lidar surveys, and various methods for displacement measurements.

The unstable area of the Åknes rockslide extends from $\approx$ 100 m a.s.l. close to the shoreline of the fjord to 900 m a.s.l. in the mountain slope (Fig. 1), where the large-scaled back scarp extends in an E-W direction (Ganerød et al., 2008). The extent of the unstable area is estimated to be 500 m across-slope and 1200 m down-slope (Figs. 1b and 2). Depth and hence volume of the entire unstable rock mass are still uncertain. Nordvik et al. (2009) discusses different scenarios with varying depths of the basal sliding plane from 40 to 190 m resulting in volume estimates of 20 to 85 million m^3. Kveldsvik (2008) suggests from slope stability analysis a deep sliding plane at 120 m depth and a volume of 60-80 million m^3. Prominent slide scars on the rockslide (Fig. 2) indicate rockslide activity already in the past centuries (Blikra, 2008; Kveldsvik et al., 2008).

Geological settings

Åknes is situated within the Western Gneiss Region, where gneissic rocks from the Proterozoic dominate (Braathen et al., 2004). Bedrock of the unstable slope comprises different types of gneiss, but are mainly medium grained granitic to dark grey biotite-bearing granodiorite gneiss (Ganerød et al., 2008). In the upper central part of the rockslide, the planar or gently folded foliation dips $30 - 35°$ towards the southeast, mainly sub-parallel to the topography. Fractures run along the foliation within biotite-rich layers. Some of them act as sliding planes (Braathen et al., 2004; Ganerød et al., 2008). Such sliding planes breach the surface at the toe zone and in the central part of the rockslide (Fig. 2) and are also observed in boreholes at different depth levels.

In the upper central part of the rockslide a WNW to ESE striking 10 m high cliff is formed (Fig. 2). Due to extensional movements in this region, steeply dipping tension fractures are exposed at some locations both north and south of the cliff (Fig. 2). The exposed tension fractures strike mainly E-W to ESE-WNW and appear as up to 1 m wide openings in the bedrock or depressions in the blocky colluvial debris (Ganerød et al., 2008; Blikra, 2008). For some of the tension fractures north of the cliff dip angles were determined that are in the range of $60 - 90°$ towards the N (Fig. 2). Because large areas are covered by debris it is difficult to trace the tension fractures over larger distances across the surface. Wide-spread

areas with debris coverage are particularly observed above the cliff (Fig. 2), however, the region below the cliff is covered by tight vegetation that may hide both additional tension fractures and areas with debris deposits.

Apart from the tension fractures, Ganerød et al. (2008) classified three fracture sets from outcrops in the rockslide area. In addition to the foliation-parallel faults, two steeply dipping fracture sets that strike predominantly E-W and N-S have been identified. The foliation-parallel fracture set shows the highest fracture density (on average 17 fractures per m) and the largest continuity (average fracture length of 6-10 m).

Surface movements have been determined both from spot measurements (extensometers, laser distance meters, GPS and electronic theodolite with integrated distance meter) (see Fig. 2) and area-based techniques like aerial and terrestrial laser scanning (Oppikofer et al., 2008), photogrammetry (Kveldsvik et al., 2006) and radar interferometry. Average displacement rates ($\approx$ 2-4 cm/year for the largest part of the rockslide) have been quite similar over the past 20 years, with no general tendency of acceleration (Kveldsvik et al., 2006). However, water infiltration is known to have a large impact on the movements, such that their rates can increase with up to a 1 mm/day by a factor of 10 during snow melt or periods with high precipitation (Blikra, 2008). In general, displacement rates are highest close to back scarp and decreasing towards the toe zone and the eastern part of the rockslide and movement patterns show that individual blocks move separately in the highly fragmented rockmass (Ganerød et al., 2008; Kveldsvik, 2008; Oppikofer et al., 2008). At the western flank immediately underneath the back scarp the rock mass moves fastest with velocities up to $\approx$ 14 cm/year in SW to SSW directions (Fig. 2). In the upper central part the slope is creeping at 2-4 cm/year in a SSE direction (Ganerød et al., 2008). In the lower part of the rock slope no significant lateral displacements are observed, but positive elevation changes of the order of 1 to 3 cm/year are associated with compressional movements (Ganerød et al., 2008). Compression is also associated with outcoming blocks in the toe zone and in the eastern part of the rockslide (see Ganerød et al., 2008; Blikra, 2008, and Fig.2).

In a multi-tracer test experiment, tracers were infiltrated at different locations along the back scarp and in boreholes. Water probes were then taken from all accessible springs and

creeks (Fig. 2) within the rockslide area (Frei, 2008). Very high flow rates (peak velocities up to 17.4 m/h between the infiltration and spring locations) were observed, indicating that the unstable rock slope is highly permeable due to intense fracturing. Also low conductivities of water taken from the springs (<100 μS/cm) suggest short residence time of the water in the rock and, hence, high permeability (Frei, 2008). Water infiltrated at points located close to each other were often observed at very different spring levels. So, a tracer injected in the borehole B1 was partly observed at the springs I and II in the central part of the rockslide (Figs. 2), but a tracer injected in the borehole B2 was not detected at these springs, but observed at lower springs at the toe zone of the rockslide. Frei (2008) and Thoeny (2008) concluded from such tracer test results that several preferential groundwater flow paths exist at different depths levels of the rockslide.

[Figure 2 about here.]

[Figure 3 about here.]

Boreholes

Seven boreholes were drilled at three locations across the rockslide (see sites B1, B2 and B3 in Figs. 2 and 3). For each location, we only present here the results from the most recent $\approx$ 200 m deep boreholes that were vertically drilled in 2006. They have been investigated with natural gamma and sonic logs (see Fig. 4b and c). Furthermore, water flow (see Fig. 4d and e), temperature and conductivity of the water were measured with depth (Elvebakk, 2008; Thoeny, 2008). Water flow was dynamically measured with an impeller flowmeter that was moved upward and downward with constant speed. The average of both measurements was considered as the water flow in the boreholes. Water levels in the boreholes show rapid daily fluctuations and vary with seasonal changes of the infiltration rate up to 5 m (Thoeny, 2008; Blikra, 2008). Therefore water table depths in borehole B2 were slightly different during the gamma log and sonic log ($\approx$ 44.5 m) and the flowmeter ($\approx$ 47.5 m) measurements (see Figs. 4b-d).

From drill cores largest fracturing (up to 50 fractures per meter) was determined in the unsaturated uppermost 20-50 meters of the boreholes (Fig. 4a). Although fracturing

gradually decreases with depth, also in the deeper part of the boreholes locally narrow zones of highly fractured and disrupted rock were mapped (Ganerød et al., 2007, 2008). In borehole B2 such disrupted zones up to 30 cm width were observed down to about 100 m. Below this depth no zones with significant fracturing were identified from drill cores. However, close to the bottom of the borehole B2 at 200 m depth, where no logging measurements were performed, complete loss of fluid pressure during the drilling process (L.Blikra pers. comm.) indicated the existence of open fractures at large depth. Independent of the depth range mapped fractures were mainly assigned to the foliation parallel fracture set.

Logging results shown in Fig. 4b-e are in agreement with the observations from the drill cores. So, decrease in P-velocity (e.g. velocities down to $\approx 1500\,\mathrm{m/s}$ were observed at 57, 77, 87 and 94 m depths in borehole B2) corresponds in most cases to zones having an increase in fracture frequency (see Fig. 4a). Moreover, depths with significant water in- and outflow could be associated with zones that are characterized by increased fracture frequencies (see water inflow at 77 m depth in Fig. 4d) indicating that these kind of fractures are relevant water flow paths within the unstable rockmass. Gamma logs (Fig. 4b) showed peaks with increased gamma ray activity at some fracture zones suggesting that these zones may be filled with potassium rich clayey material. However, the hydraulically active zone at 77 m in borehole B1 (Fig. 4d) is not characterized by such an peak.

Water circulation differs strongly in the boreholes. In borehole B1 (Fig. 4e) several hydraulically active fractures were identified by water inflows and outflows and high ambient flow rates were indicative for strong hydraulic head gradients in the rock mass. In contrast, in borehole B2 (Fig. 4d) no zone with significant inflow and only weaker ambient flows[1] were observed below a depth of 77 m.

Preliminary results from inclinometer measurements in the upper and middle borehole B1 and B2 indicate relative movements at several depth levels down to 120 and 80 m (M. Lovisolo, pers. comm.), although the largest movements in the borehole B2 occur at shallow

[1] Impeller flow meters are usually not able to resolve flow rates lower than $\approx 0.5\,\mathrm{m/min}$ (e.g. Crowder and Mitchell, 2002) and small diameters of 76 mm can be responsible for turbulence in the boreholes. Therefore, systematic shifts in our obtained flow rates are likely.

depths of $32 - 35$ m.

[Figure 4 about here.]

Results from the borehole B2 are particularly relevant for our investigations, because it is located in the central part of our seismic array (see Fig. 3).

3. Geophysical investigations

Already in an earlier stage of the project refraction seismic data were collected along three lines (Ganerød et al., 2008). Based on these results Ganerød et al. (2008) interpreted roughly a four-layered case of loose material on top, highly fractured unsaturated rock, fractured water saturated rock and less fractured rock. All these data sets had only a relatively limited number of shot and receiver positions (24-channels) and therefore were not able to resolve detailed structured. In addition, GPR profiles were measured with 50 MHz antennas along some parts of the geoelectric profiles (Ganerød et al., 2008). Signal penetration was with up to 40 m good, but due to the complexity of the disrupted rock mass it was challenging to interpret the complex reflection and diffraction patterns in the radar sections. However, some reflections could be identified as the top of the uppermost groundwater table down to depths of ~ 30 m and correlated well with the upper boundary of low-resistivity anomalies in the 2-D electric tomograms.

DC resistivity investigations

Geoelectric data were recorded along nine intersecting profiles (P1 - P9 in Fig. 3) during the summers of 2004, 2005 and 2006. The pattern of geoelectric lines covered the complete rockslide area, with profiles extending into the neighboring stable rock mass. The longest profiles P1 and P2 had lengths of ≈ 1500 m. They reached from the shoreline up to the stable region behind the back scarp (Figs. 3 and 5a). Four cables with an electrode spacing of 10 m were used, such that the maximum electrode spread was 800 m and the profiles had to be extended by a roll-along strategy. Six profiles (P1, P2, P3, P4, P8 and P9) crossed the area of the 3-D seismic survey.

Data were collected with the LUND multi-electrode system (Dahlin, 1993) using an ABEM Terrameter SAS 4000. Both Wenner and dipole-dipole configurations with successively increasing dipole lengths were measured on all profiles. Particularly on scree, electrode coupling had to be improved by using salt-water soaked sponges. For most measurements, the current reached 10 - 20 mA, but for few measurements of $\approx 2.5\%$ the current was not higher than 1 to 2 mA. Due to the high resistivities of the ground, the measured voltages were relatively large, such that the data were of good quality with standard deviations mainly below 1%.

[Figure 5 about here.]

[Figure 6 about here.]

Already in Ganerød et al. (2008) first results from the 2-D resistivity measurements were presented. They inverted geoelectric data with the 2-D code from Loke (2001) and from final results they were able to distinguish water-saturated and drained regions on the the Åknes rockslide. In this contribution we present both 2-D and 3-D inversion results obtained with the the BERT algorithm (Günther et al., 2006b). This algorithm uses unstructured meshes both for parametrization and forward calculations (Rücker et al., 2006). Smoothing constraints were used in the inversion as regularization. All collected geoelectric profiles were inverted with the 2-D algorithm, but only profile segments located within or close to the seismic array were jointly inverted with 3-D algorithm. The 3-D inverted data set comprised 17 970 measurements from 975 electrode positions.

The resistivity distribution derived from 2-D inversions are shown for the two profiles oriented mostly in the slope direction (P1 and P2) in Figure 5a and from two profiles (P3 and P4) crossing the rockslide from E to W in Figure 5b.

Seismic investigations

Our 3-D seismic experiment was carried out across the upper part of the unstable rock mass in the summer of 2007 (Fig. 3). Altogether 24 geophones were placed along each of the four crossing profiles (total of 96 geophones). Three profiles (Q1-Q3) ran along the slope and

one perpendicular to it (Q4). The quasi-parallel profiles Q1, Q2 and Q3 were separated by ≈ 50 m. Such a setup with most profiles oriented in the slope direction was chosen, because geophone profiles that cross fractures are better suited to resolve the associated low-velocity anomalies than profiles that run parallel to the fractures (Heincke et al., 2006) and surface observations indicated that large-scaled open fractures strike perpendicular to the slope.

Receiver spacing was 20 m for the middle profile Q2 and 10 m for the other profiles leading to geophone spread lengths of 460 m and 230 m, respectively. The larger length of profile Q2 was chosen to obtain ray coverage at greater depths, which is particularly important because the lower limit of the slope instability is still unknown. Most of the 163 shots were evenly distributed over a rectangular area of 250 x 250 m (Fig. 3), which included profiles Q1, Q3, Q4 and the middle part of profile Q2. Moreover, several shots were fired outside of the rectangle along profile Q2 (Fig. 3b). Finally, five far-offset shots were placed along an extension of profile Q2 (Fig. 3a). Three of them were located downhill of the seismic survey and the other two uphill in the stable part of the rock mass behind the back scarp (see Fig. 3).

As sources explosives with charges of 100 to 400 g were used. They were placed in 50 cm deep boreholes drilled mainly into bedrock. Data collection was performed with four 24-channel GEODE recording units from GEOMETRICS. Data quality was generally good and for the majority of traces first arrivals could be picked with an accuracy of ≈ 3 ms. For some shots located on debris, accurate first arrival-time picking was not possible for larger offsets because of energy loss. Altogether, 11 276 first-arrival picks were used for the tomographic 3-D inversion. Figure 6a shows a typical shot gather (location of the shot is highlighted in Fig. 3) and Figure 6b shows apparent P-wave velocities versus shot-receiver offsets for all picked first arrival-times.

[Figure 7 about here.]

Data were inverted using a smoothness constrained minimization algorithm on a tetrahedral mesh (Günther et al., 2006a). For the forward calculation a Dijkstra algorithm (Dijkstra, 1959) was used that restricts the ray paths to element boundaries. Although this leads to

inaccuracies for short offsets and weak velocity contrasts, these inaccuracies are limited by using highly refined meshes in the shallow part of the model.

Meshes and coverage

The topography model for both the 2-D and 3-D investigations was determined from electrode, geophone and shot positions and points from a digital elevation model (Derron et al., 2005). This topography model was then used as input for the tetrahedral mesh generator. For the 3-D resistivity and velocity models, we used the same mesh to simplify the comparison. Final parametrization for the 3-D models contained about 31 000 cells with edge lengths from a few centimeters close to the surface up to some 10 meters at depth. In all inversions, smoothness constraints were applied between neighboring cells. Thereby, the direction perpendicular to the topography was less constrained to account for possible layered structures.

For most of the 2-D geoelectric profiles, relatively high RMS values were obtained for the data misfit (Fig. 5). This can be explained by the chosen robust (L1-norm) data weighting (Claerbout and Muir, 1973), where the chi-square misfit is low, but the RMS is dominated by single outliers. Main reasons for such outliers are probably three-dimensional effects in the 2-D sections associated with highly complex subsurface conditions and the undulating topography on the rockslide. Such 3-D effects also explain observed discrepancies in resistivities at the intersection points of different geoelectric profiles (consider e.g. resistivities in profile P1 and P4 at their intersection point in Fig. 5).

The 3-D resistivity data were finally fitted with a relative RMS of 23%, and seismic data were fitted with an absolute RMS of ≈ 4 ms. Whereas the latter is comparatively low, the misfit of the electrical data is high compared to other surveys. As for the 2-D profiles, the high RMS values can partly be explained by the used robust data weighting, but also by a strong regularization. Because small-scale anomalies apart from the profiles cannot be resolved by the sparse profile layout, a high smoothing was chosen, such that only dominant larger structures were determined.

The coverage for the final 3-D resistivity and seismic tomograms are shown in the Fig-

ures 7c and d, 8d-f and 9d-f. Coverage in the geoelectric tomograms is presented as the logarithm of the summed (absolute) sensitivities in each inversion cell and coverage in the seismic tomograms is presented as the summed lengths of all ray segments in each inversion cell.

Referring to Gharibi and Bentley (2005), it can be meaningful to make a 3-D inversion of 2-D profiles in regions where dense patterns of crossing lines exist. This is the case for most of the area where we performed the 3-D seismic experiment (see Fig.3b). Accordingly, the coverage in our resistivity model is high and uniformly distributed at greater depths of 30-100 m (see Figs. 8e and f). Only in the uppermost 20 m of the model, does the arrangement of measurements along profiles cause irregular coverage (see Figs. 7c and 8d) with significantly higher resolution close to the lines than in between. As a consequence, shallow high-resistivity anomalies, which can be associated with a thin layer of scree material at the surface, appear only in the well-resolved regions in the neighborhood of the electrodes (Fig. 7a and 8a). In contrast, in poorly resolved regions away from the lines, spurious artifacts occur at shallow depths. These are caused by the projection of low-resistivity anomalies located in greater depths. Gharibi and Bentley (2005) observed similar artifacts at shallow depths if lines are separated by more than four times the electrode spacing. In our case electrode spacing was 10 m and the profiles are separated by up to 80 meters.

In contrast, the ray coverage of the seismic tomography is more homogeneously distributed in all depth intervals due to the 3-D experimental setup (Fig. 9). Lower ray coverage in the uppermost $30-40$ m relative to that at larger depths of $50-100$ m is related to the significantly smaller average size of the tetrahedrons close to the surface (Figs. 7d and 9d-f). High ray coverage was obtained down to a depth of $\approx 100-120$ m (Figs. 7d and 9f).

We point out that coverage is only a coarse measure for resolution and that resolution estimates based on coverage can significantly deviate from the true resolutions. Therefore, low-transparent regions in the Figures 7,8 and 9 represent only roughly well-resolved parts of the tomograms.

[Figure 8 about here.]

[Figure 9 about here.]

[Figure 10 about here.]

4. Results and discussion

2-D geoelectric measurements

We can roughly divide the shallow rock mass into different zones by means of the 2-D resistivity inversion results. Mainly in the middle and upper part of the tomograms of profiles P1 and P2 (Fig. 5a) and in the middle and western part of the tomograms of profiles P3 and P4 (Fig. 5b), a thin highly resistive near-surface layer ($> 20\,\mathrm{k\Omega m}$) with a varying thickness (usually < 20 m, but in the upper part of the slope up to 40 m) is observed that can be related to colluvial material and drained fractured rock. Underneath, zones of lower resistivities ($\approx 5 - 14\,k\Omega\mathrm{m}$) indicate increased water content in the fractured rock. In the upper part (see profiles P1 and P2), the central part (see profiles P2 and P4) and in the western part (see profile P3 and P4) of the rockslide, these lower resistivity zones appear as elongated, mainly surface-parallel anomalies with a varying thickness of $25 - 60\,\mathrm{m}$. Springs are observed at several locations, where these anomalies approach the surface. This is the case in the toe zone, in the central part and western part of the rockslide body. At first glance, one may link these anomalies to foliation parallel fracture sets because of the reasons mentioned in section 2. However, since the rock mass is also heavily intersected by fractures with other orientations it can be assumed that the elongated low-resistivity anomalies represent the net effect of all open fractures.

Along some parts of the profiles, the resistivity underneath these low-resistivity anomalies increases again. This is either related to unsaturated conditions or less fracturing and, hence, lower water content in the bedrock. In other parts (see profiles P1 to P4) the relatively low resistivities continue to greater depths, indicating deeper groundwater paths (Blikra, 2008). Because these steeply dipping anomalies touch the lower boundary of the resistivity models, the actual origin of the associated groundwater cannot be resolved by the geoelectric measurements. For the low-resistivity anomalies in the sections P1 and P2 closest to the

shoreline (Fig. 5a), saltwater from the fjord has surely an effect and these anomalies are not necessarily associated with groundwater from the rockslide.

At the eastern boundaries of the rockslide a distinct resistivity increase from the unstable region towards the stable region is present in the 2-D sections of profiles P3 and P4 (Fig. 5b) indicating that the intact rockmass has lower water content related to less fracturing. Such a clear contrast is not present in the 2-D sections in the region around the backscarp (Fig. 5a) and along the western rockslide boundary (Fig. 5b). However, in 3-D inversion results from all measured geoelectric data on the rockslide (not presented here) clearly higher resistivity values ($> 17.5\,\mathrm{k\Omega m}$) are observed in the intact rock mass above the backscarp than in the unstable rock mass immediately below the backscarp. This is an indication that interpretations based on two-dimensional data have to be made carefully in regions characterized by such complex subsurface conditions.

3-D surface geophysical investigations

Results from the 3-D geophysical investigations allow us to make a more detailed interpretation of the upper central part of the rockslide. In the uppermost 50 m, P-wave velocities in the 3-D seismic tomogram are $v_p < 3500\,\mathrm{m/s}$, which is generally very low for gneissic rock (Figs. 7b, 9a and b and 10). This suggests that the whole shallow rock mass in this area is heavily fractured, in agreement with surface and borehole observations (Ganerød et al., 2008). Within this disrupted rock mass, mainly three shallow anomalies with particularly low velocities of $v_p < 1400\,\mathrm{m/s}$ stand out. Two of them run parallel to each other and are oriented perpendicular to the slope in WNW-ESE direction. They are separated by $\approx 50\,\mathrm{m}$ and located immediately above and below the cliff (see L and U in Figs. 7b, 9a and 11c and d). The third anomaly runs in a NNW-SSE direction in the northeastern part of the seismic survey and merges with the anomaly (U) at its southern edge (see D in Fig.9a). All anomalies extend from the surface down to a depth of $\approx 25\,\mathrm{m}$. Underneath the two parallel low-velocity anomalies (L) and (U), there are two parallel anomalies with relatively low resistivities ($<13\,\mathrm{k\Omega m}$) (see Figs 7a, 8b and c and 11a and b). Also underneath the southern part of the low-velocity anomaly (D) a low-resistivity anomaly is observed, how-

ever, not in the northern part. In areas with high model coverage, the upper boundaries of the resistivity anomalies are predominantly located in a depth range of 20-50 m (Figs. 7a, 8 and 10). For the low-resistivity anomalies the decrease in resistivities down to $\approx 10\,k\Omega$m at depths of about 50 m coincides with a significant increase in velocities up to $v_p \approx 3200\,\mathrm{m/s}$ (see continuous line in Fig. 10). Also in many regions with no pronounced low-velocity and low-resistivity anomalies, resistivity decreases with depth, however, less significant than along the anomalies (see dashed line in Fig.10 and well resolved regions in Fig.7a).

[Figure 11 about here.]

[Figure 12 about here.]

The low-velocity and low-resistivity anomalies can be explained by elongated tension fractures that are dry close to the surface and water-saturated at larger depths. So, the pair of parallel low-velocity anomalies (L) and (U) are located in a region where tension fractures were mapped (Figs. 11a and c) and can be associated with the continuation of these surface fractures at depth. No surface fractures were mapped along the low-velocity anomaly (D), but significant amount of debris covers the bedrock here and potential tension fractures may remain undetected on the surface.

Since the water table in the nearby borehole B2 was at $\approx 45\,\mathrm{m}$, it can be assumed that air filled fractures above this depth are responsible for the very low P-wave velocities in the disrupted rock mass in general (Heincke et al., 2006) and along the tension fractures in particular. Below this depth, the fractures are water-saturated and have a much weaker impact on the overall velocity, resulting in a decreased velocity contrast and an increased average velocity (see Figs. 7b and 9b). Water within fractures also explains the decreased resistivities at depths below 20 to 50 m and the appearance of the relatively low-resistivity anomalies along the tension fractures. Since the resistivities of a few kΩm are still very high, it can be assumed either that fracture widths and hence water volumes are small or that the water is not very conductive (Frei, 2008).

It can be observed from figures 7a and b and 11a and c that the low-resistivity anomalies (L) and (U) are not located directly underneath the associated low-velocity anomalies,

but are slightly shifted in downhill and uphill direction relative to the related low-velocity anomalies, respectively. These lateral shifts of the low-resistivity anomalies suggest that the tension fractures are not exactly vertical. For comparison tension fractures mapped at the surface have dips of $60 - 90°$ towards the N (see Ganerød et al., 2008, and Fig. 11). At the eastern part of survey the low-resistivity anomalies (U) and (L) and the low-resistvity anomalies (U) and (D) merge (Figs .8b and c, 9a and c and 11) suggesting that associated tension fractures intersect in this region.

Interpretation in terms of tension fractures is in agreement with surface observations and displacement measurements. So, the unstable rockslide body is fragmented by intense fracturing into a large number of individually moving blocks (Ganerød et al., 2008; Kveldsvik, 2008; Oppikofer et al., 2008). The horizontal component of the displacement vectors close to the tension fractures (see Fig. 2) change their orientations from SSE close to the borehole B1 in the west to ESE east of the borehole B2 and such a movement pattern can explain that fractures mainly open in a downhill direction (with decreasing spreading rates towards the east) as interpreted from the surface geophysical results.

Because of the inherently limited resolution of both tomographic methods more detailed interpretations of these anomalies in the geophysical models are not reasonable without performing extensive resolution analysis or synthetic modeling. It cannot be answered if individual fractures or disrupted zones of up to few meter thickness are responsible for the observed anomalies and where and in which way fractures are exactly connected. Also accurate dip angles for the tension fractures are not determinable.

Below the groundwater table the 3-D seismic refraction tomography is not able to resolve thin surface-parallel low velocity layers that are observed in the boreholes (see section 2) and are associated with foliation parallel fracture zones. In contrast, velocities from the seismic tomography gradually increase with depth and velocity values of $\approx 2500 - 4500\,\mathrm{m/s}$ in the depth range of $50 - 90\,\mathrm{m}$ (Fig. 7b, 9a-c and Fig. 10) can be explained by a net effect of velocities from intact rock and disrupted zones (Fig. 4). Its is remarkable that velocities

in this depth range are often slightly lower in regions where no low-resistivity anomalies are present (see Fig. 10 and compare depth slices from Figs. 8 and 9 at 70 meters). One plausible explanation would be that not all fractures at some distance from the tension fractures are water-filled and air-fill leads to a more significant velocity reduction here. Below a depth of about 100 m seismic velocities are with $4500 - 5500$ m/s typical for intact gneissic rocks (Fig. 7b and Fig. 10). Also high apparent P-wave velocities of $3500 - 4000$ m/s at offsets > 400 m indicate that refracted P-waves of far-offset shots run partly through intact rock (Fig. 6b).

Below 70 meters resistivity increases in most regions slowly with depth (Fig. 10), which is probably related to less water content due to less intense fracturing of the rocks with depths (see Fig. 4a and c). However, in region where the low-resistivity anomalies are present resistivities remain relatively low even in larger depths (see Fig. 10).

Linking the geophysical results to the hydraulic system

By comparing the 2-D and 3-D geoelectric results, we see that the deep low-resistivity anomalies in the 2-D tomograms of P1, P2 and P3 (see A, B and C in Fig. 5) coincide with low-resistivity anomalies (L) and (U) (Fig. 11a) in the 3-D tomogram. This indicates that the associated tension fractures continue down to depths of at least $80 - 100$ m. Hence, it is very likely that the tension fractures intersect other differently oriented fractures at various depth levels, allowing groundwater to down-well or up-well and to penetrate into other open fractures. In this way, tension fractures can significantly change the main groundwater flow paths in the rockslide body.

Because the 3-D resistivity tomography does not have the resolution to identify where and which individual fractures are water filled from the tension fractures, results from multi tracers tests (Frei, 2008) and impeller flowmeter measurements are very helpful to test this hypothesis:

- Tracers infiltrated in the boreholes B1 and B2 were observed at different spring horizons on the rockslide (see section 2). This means that between the two boreholes B1 and B2 cross-cutting hydraulic permeable structures are required allowing the water to

change the depth level of its preferential groundwater path. The detected steeply dipping tension fractures are the most plausible candidates for such structures.

- From the arrangement of the upper low-resistivity and low-velocity anomalies (U) (see Figure 11) it can be assumed that the associated tension fracture is located uphill relative to the two boreholes B1 and B2. Water that infiltrates from the surface into this tension fracture may enter other fractures (e.g. foliation parallel fractures) and is observed as inflow in the boreholes. Although not understood in detail it is remarkable that the water circulation in the boreholes B1 and B2 is strongly different over a relative short distance of ≈ 250 m (Fig.4d and e) suggesting that the hydraulic system is significantly changed by the tension fractures.

In the south-eastern part of the investigated area the low-resistivity anomaly approaches the surface (see Fig. 11a and b). This suggests that outflowing water at the nearby spring I is associated with this anomaly. At first glance, this observation seems to contradict our interpretation, because the resistivity anomalies (U) and (L) are connected in the southern part of the survey, but tracer infiltrated at borehole B2 is not observed at spring I. However, because of the limited resolution of the geoelectric tomography, it is indeed possible that separate water flow paths are located so close to each other that they appear as one anomaly. Such a scenario is also not unexpected considering the 2-D geoelectric section P1 in the region between the borehole B2 and the spring I (see Fig. 5a). The low-resistivity anomalies are thick here and partly touch the bottom of the geoelectric sections. Multiple water flow paths at different depths levels that are not resolvable as separate water flow paths are likely here.

Considering the monotonically velocity increase with depths in the seismic tomogram (Fig. 7b) and the decrease of fracturing with depths from drill cores and borehole logging (Fig. 4a and c), the existence of the open hydraulically permeable fractures at 200 m depths (see section 2) in the borehole B1 is not expected. However, the deep low-resistivity anomalies from the 2-D sections suggest water flow paths and hence also open fractures (in this case water-saturated) at greater depths. Because of limited resolution, relatively thin fractures

at such depths are unlikely to be detected by the surface seismic investigations.

[Figure 13 about here.]

Relating geophysical results to the depths of the slope instability

It is unfortunately not possible to determine the lower boundary of the highly fractured mass from the 3-D seismic tomogram, because no sharp velocity contrast is observed that would indicate a border between highly fractured and intact rock. Instead, velocities gradually increase below the water table (Figs. 7b and 9b and c) indicating that the velocity contrast between the (water-saturated) unstable and underlying stable mass is too small to be resolvable. Velocities of less than 3500 m/s are surely too low for intact gneissic rock, such that a minimum depth of 60-70 m can be assumed for the disrupted rock mass from the seismic measurements. At depths of ≈ 100 m velocities are with ≈ 5000 m/s in the same range as velocities from the sonic logs in depths with no pronounced fractures (Fig. 4c) suggesting that the rockmass is intact at this depth. However, we cannot state for certain that the rockmass is stable at this depth.. It is possible that open fractures that are located deeper than maximum resolution depths of the surface geophysical methods also act as sliding planes.

Based on the results of surface geophysics and borehole logging a possible geological model from the upper central part of the rockslide is sketched in Figure 12.

5. Conclusions

A combination of 3-D seismic refraction and electrical resistivity tomography on the Åknes rockslide demonstrates their potential to detect three-dimensional weakened zones. Furthermore a combination of the tomograms with the results of tracer tests and borehole data gives an indication of the geo-hydraulic behavior of fractures. From the seismic data, the upper drained zone of two parallel extension fractures can be associated with shallow low-velocity anomalies ($<$1400 m/s). From the geoelectric data, the zone of the extension fractures below the groundwater table can be associated with low resistivities ($<$13 kΩm)

compared to the surrounding bedrock, indicating that fractures are water-saturated. In combination with results from borehole logging, there are strong indications that the tension fractures are cross-cutting several other water-saturated fracture zones. Tension fractures enable water to infiltrate and may allow changes of their depth levels and even changes of their preferential flow paths. However, to obtain a thorough understanding of the water regime, our surface geophysical data have to be more closely correlated with results from tracer tests (Frei, 2008) and dynamic fluid electric conductivity logging (Thoeny, 2008) in the future.

Typically for inversion methods, not all parts of the model are well resolved and sharp boundaries (e.g. the tension fracture edges or the upper border of the ground water level) are smoothed out in the resultant models. To account for those shortcomings we intend to perform a structural joint inversion of our two 3-D data sets. Such structural joint inversion algorithms link two (or more) otherwise independent inversions via structural similarities (e.g. Gallardo and Meju, 2003; Günther et al., 2006a; Paasche and Tronicke, 2007) and can finally provide a more distinct combined image of the rockslide.

Acknowledgements

First of all, we appreciate the work of Stian Græsdal from the Stranda Municipality, Norway, who was a great help in all field campaigns. We thank also Hui Lu helping us as field assistant in the seismic campaign. Thank to Kjell Jogerud and Tore Bereng from the Åknes/Tafjord project and other people from the Stranda Municipality for all kind of logistic support that was required to run successfully these field campaigns in such a remote area. We thank Denis Jongmans (LIGRIM, Grenoble), Walter Wheeler (CIPR, Bergen) and Svein Erik Hamram (University of Oslo) for their support with seismic equipment. We appreciate also the support from the project leader Lars Blikra (NGU, Trondheim), Isabelle Lecomte (Norsar/ICG, Oslo), Cristian Frei (ETH Zurich) and Michael Roth (Norsar, Lillestroem). We thank Lars Blikra, Reto Thoeny (ETH-Zurich) and Max Moorkamp (IFM-GEOMAR) for helpful comments. Thanks to two reviewers, Andreas Pfaffhuber and an anonymous person, and the associated editor Alan G.Green for reviewing and improving the manuscript. The

project was funded by the Åknes/Tafjord project, ICG-International Center of Geohazards (ICG) and the Geological Survey of Norway (NGU).

References

Batayneh, A., Al-Diabat, A., 2002. Application of a two-dimensional electrical tomography technique for investigating landslides along the Amman-Dead Sea highway, Jordan. Environmental Geology 42, 399–403.

Blikra, L., 2008. The Åknes rockslide; monitoring, threshold value and early-warning. In: 10th International Symposium on Landslides. Xi'an, China.

Blikra, L., Longva, O., Harbitz, C., Løvholt, F., 2005. Quantification of rock-avalanches and tsunami hazard in Storfjorden, western Norway. In: Senneset, K., Flaate, K., Larsen, J. (Eds.), Landslides and Avalanches. ICFL 2005 Norway, Taylor & Francis Group, London, pp. 57–64.

Braathen, A., Blikra, L., Berg, S., Karlsen, F., 2004. Rock-slope failures of Norway; type, geometry, deformation mechanisms and stability. Norwegian Journal of Geology (NGT) 84, 67–88.

Claerbout, J., Muir, F., 1973. Robust modeling with erratic data. Geophysics 38, 826–844.

Crowder, R., Mitchell, K., July 2002. Spinner Flowmeter Logging: A Combination of Borehole Geophysics and Hydraulics. In: Arizona Hydrological Societies Well Design and Installation Workshop. Phoenix, Arizona.

Dahlin, T., 1993. On the Automation of 2D Resistivity Surveying for Engineering and Environmental Applications. Ph.D. thesis, Department of Engineering Geology, Lund Institute of Technology, Lund University, ISBN 91-628-1032-4.

Derron, M., Blikra, L., Jaboyedoff, M., 2005. High resolution digital elevation model analysis for landslide hazard assessment (Åkerneset, Norway). In: Senneset, K., Flaate, K., Larsen, J. (Eds.), Landslide and Avalanches. ICFL 2005 Norway.

Dijkstra, E. W., 1959. In Numerische Mathematik. Ch. A note on two problems in connexion with graphs, p. 269-271.

Elvebakk, H., 2008. Borehullslogging (Well logging), Åknes, Stranda kommune, NGU Report 2008.030, Geological Survey of Norway (NGU), In Norwegian.

Frei, C., 2008. Groundwater flow at the Åknes rockslide site (Norway) - results of a multi-tracer test. Ph.D. thesis, ETH Zurich, Switzerland.

Gallardo, L., Meju, M., 2003. Joint two-dimensional dc resistivity and seismic travel time inversion with cross-gradients constraints. Journal of Geophysical Research 109, B03311.

Ganerød, G., Grøneng, G., Aardal, I., Kveldsvik, V., 2007. Logging of drill cores from seven boreholes at

580 Åknes, Stranda municipality, Møre and Romsdal County, NGU Report 2007.020. Geological Survey of
581 Norway (NGU).
582 Ganerød, G., Grøneng, G., Rønning, J., Dalsegg, E., Elvebakk, H., Tønnesen, J., Kveldsvik, V., Eiken, T.,
583 Blikra, L., Braathen, A., 2008. Geological model of the Åknes Rockslide area, western Norway. Engineering
584 Geology 102, 1-18.
585 Gharibi, M., Bentley, R., 2005. Resolution of 3-D electrical resistivity images from inversions of 2-D orthog-
586 onal lines. Journal of Environmental and Engineering Geophysics 10, 339–349.
587 Günther, T., Bentley, L., Hirsch, M., 2006a. A new joint inversion algorithm applied to the interpretation of
588 dc resistivity and refraction data. In: Ext. abstr. XVI. Conference on Computational Methods for Water
589 Resources. Copenhagen.
590 URL `http://www.cmwr-xvi.org`
591 Günther, T., Rücker, C., Spitzer, K., 2006b. Three-dimensional modelling and inversion of DC resistivity
592 data incorporating topography - II. Inversion. Geophys. J. Int. 166, 506–517.
593 Godio, A., Strobbia, C., De Bacco, G., 2006. Geophysical characterisation of a rockslide in an alpine region.
594 Engineering Geology 83, 273–286.
595 Hack, R., 2000. Geophysics for slope stability. Surveys of Geophysics 21, 423–448.
596 Havenith, H.-B., Jongmans, D., Faccioli, E., Abdrakhmatov, K., Bard, P., 2002. Site effect analysis around
597 the seismically induced Ananevo Rockslide, Kyrgyzstan. Bulletin of the Seismological Society of America
598 92 (8), 3190–3209.
599 Heincke, B., Maurer, H., Green, A., Willenberg, H., Spillmann, T., Burlini, L., 2006. Characterizing an
600 unstable mountain slope using shallow 2D and 3D seismic tomography. Geophysics 71, B241–B256.
601 Jongmans, D., Garambois, S., 2007. Geophysical investigation of landslides: a review. Bulletin de la Société
602 Géologique de France 178 (2), 101–112.
603 Jongmans, D., Hemroulle, P., Demanet, F., Renardy, F., Vanbarant, Y., 2000. Application of 2D electrical
604 and seismic tomography techniques for investigating landslides. European Journal of Environmental and
605 Engineering Geophysics 5, 75–89.
606 Kveldsvik, V., 2008. Static and dynamic stability analyses of the 800m high Åknes rock slope, western
607 norway. Ph.D. thesis, NTNU Trondheim, Norway.
608 Kveldsvik, V., Eiken, T., Ganerød, G., Grøneng, G., Ragvin, N., 2006. Evaluation of movement data and
609 ground conditions for the Åknes rock slide. In: Proceedings of International Symposium on Stability
610 of Rock Slopes in Open Pit Mine and Civil Engineering. The South African Institute of Mining and
611 Metallurgy (SAIMM), pp. 279–299.
612 Kveldsvik, V., Nilsen, B., Einstein, H. H., Nadim, F., 2008. Alternative approaches for analyses of a 100,000
613 m^3 rock slide based on barton-bandis shear strength criterion. Landslides 5, 101–112.

Lebourg, T., Binet, S., Tric, E., Jomard, H., El Bedoui, S., 2005. Geophysical survey to estimate 3D sliding surface and the 4D evolution of the water pressure on part of a deep seated landslide. Terra Nova 17, 399–406.

Loke, M., 2001. Resqinv version 3.4. geoelectrical imaging 2d and 3d. instruction manual. (10.15.2004).

McCann, D., Foster, A., 1990. Reconnaissance geophysical methods in landslide investigations. Engineering Geology 29, 59–78.

Méric, O., Garambois, D., Jongmans, M., Wathelet, M., Chatelain, J., Vengeon, J., 2005. Application of geophysical methods for the investigation of the large gravitational mass movement of Séchilienne, France. Canadian Geotechnical Journal 42, 1105–1115.

Nordvik, T., Grøneng, G., Ganerød, G., Nilsen, B., Harding, C., Blikra, L., 2009. Geovisualization, geometric modeling and volume estimation of the Åknes rockslide, Western Norway. Bull. Eng. Geol. Environ.

Oppikofer, T., Jaboyedoff, M., Blikra, L., Derron, M.-H., 2008. Characterization and monitoring of the Åknes rockslide using terrestrial laser scanning. In: Proceedings of the 4th Canadian Conference on Geohazards: From Causes to Management. pp. 211–218.

Paasche, H., Tronicke, J., 2007. Cooperative inversion of 2D geophysical data sets: A zonal approach based on fuzzy c-means cluster analysis. Geophysics 72, A35–A39.

Rücker, C., Günther, T., Spitzer, K., 2006. Three-dimensional modelling and inversion of DC resistivity data incorporating topography - I. Inversion. Geophys. J. Int. 166, 496–505.

Spillmann, T., Maurer, H., Green, A., Heincke, B., Willenberg, H., Husen, S., 2007. Microseismic investigation of an unstable mountain slope in the Swiss Alps. Journal of Geophysical Research 112 (B7), B07301.

Supper, R., Römer, A., Jochum, B., Bieber, G., Jaritz, W., 2007. A complex geo-scientific strategy for landslide hazard mitigation - from airborne mapping to ground monitoring. Advances in Geosciences 14, 1–6.

Thoeny, R., 2008. Dynamic fluid electric conductivity logging for identification and characterization of preferential groundwater flow in the Åknes rockslide (Norway). Ph.D. thesis, ETH Zurich, Switzerland.

List of Figures

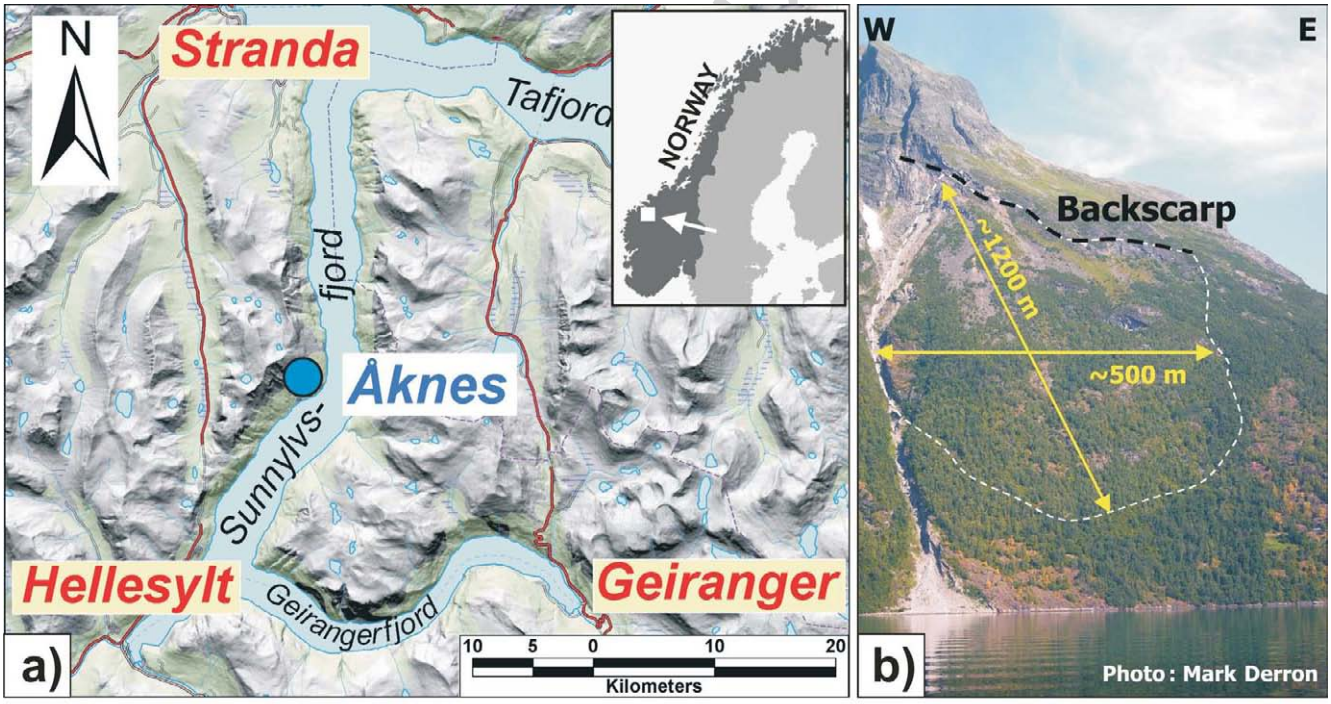

Fig.1 Heincke et al. 2009

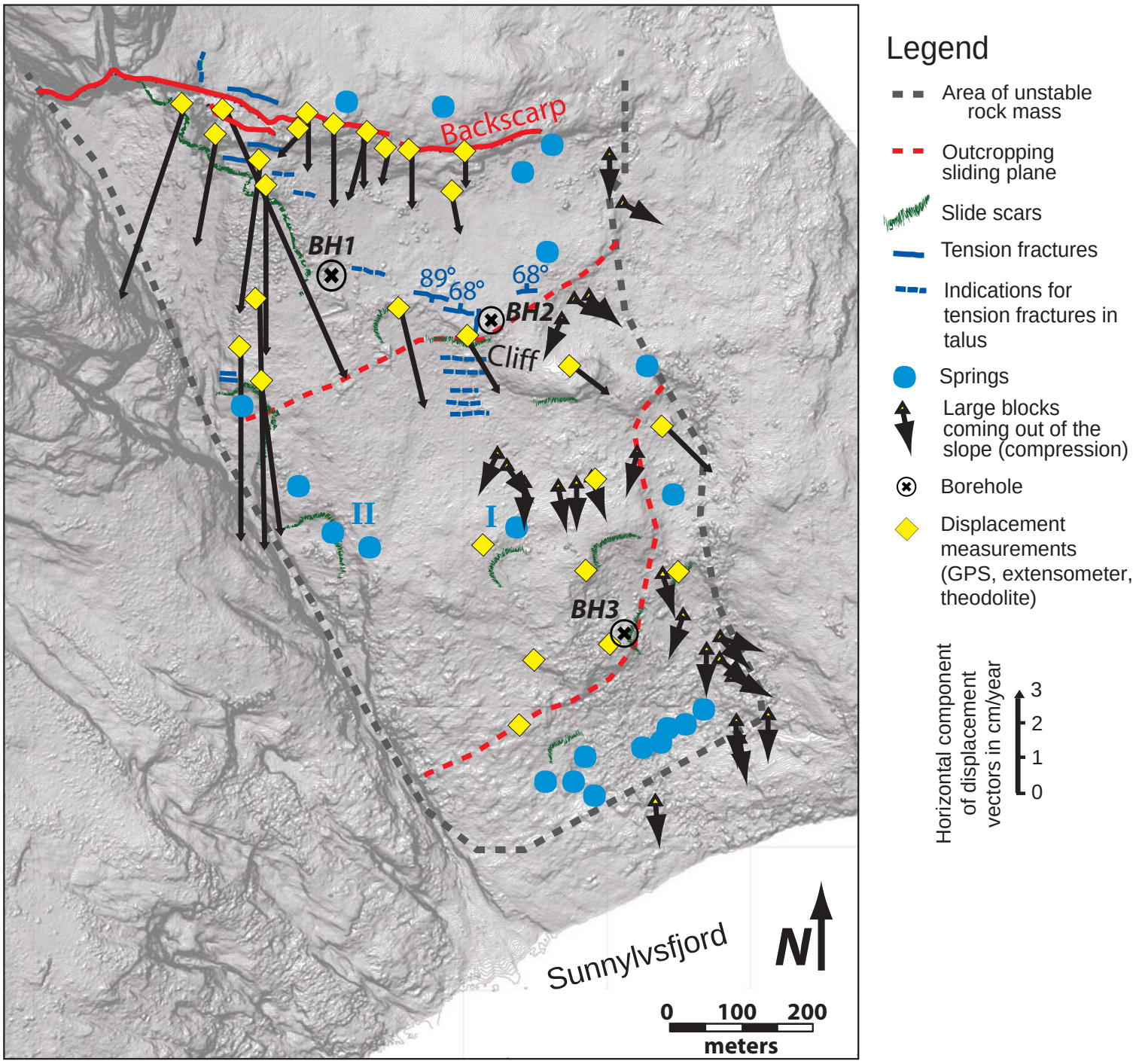

Heincke et al., 2009 Figure 2

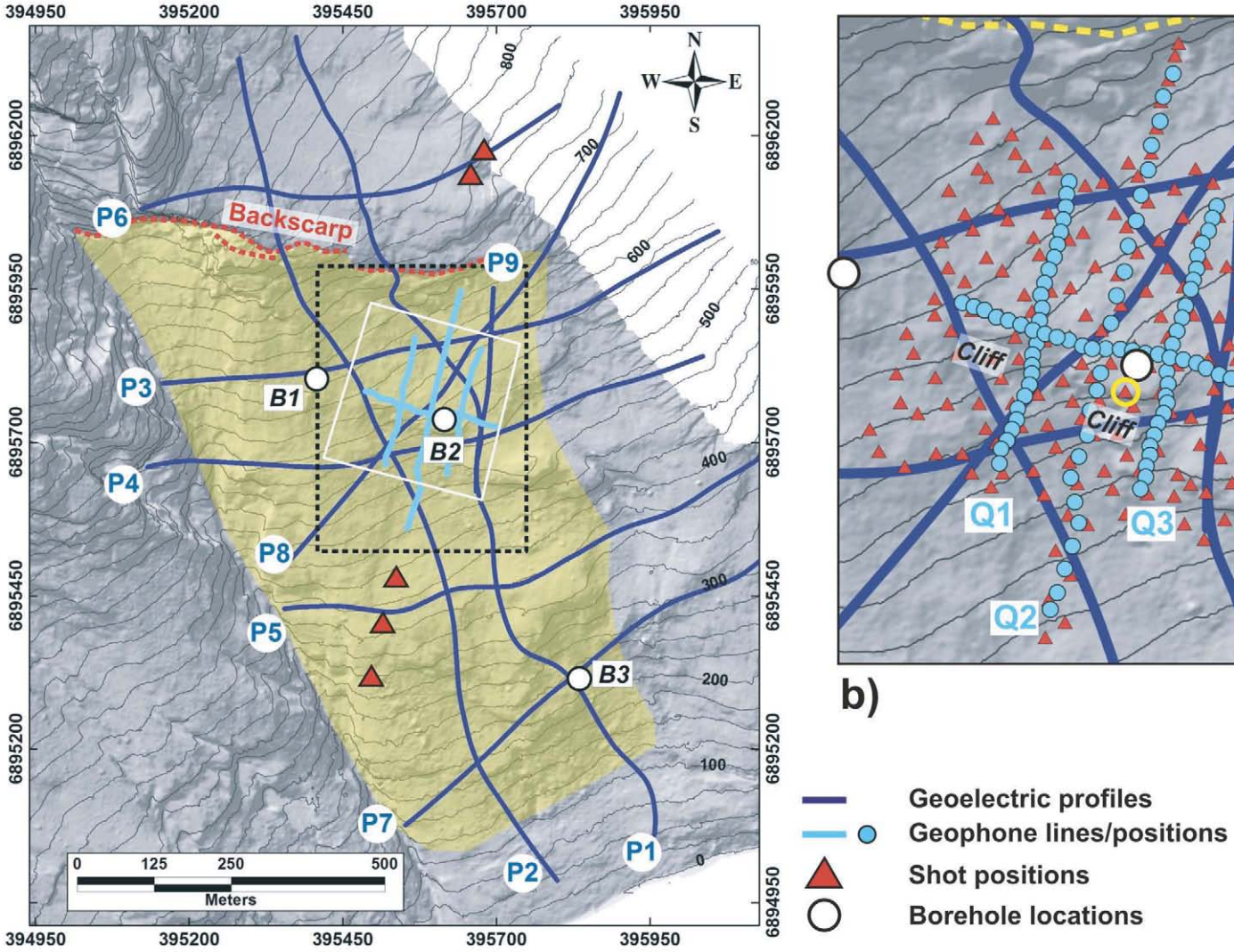

Fig.3 Heincke et al. 2009

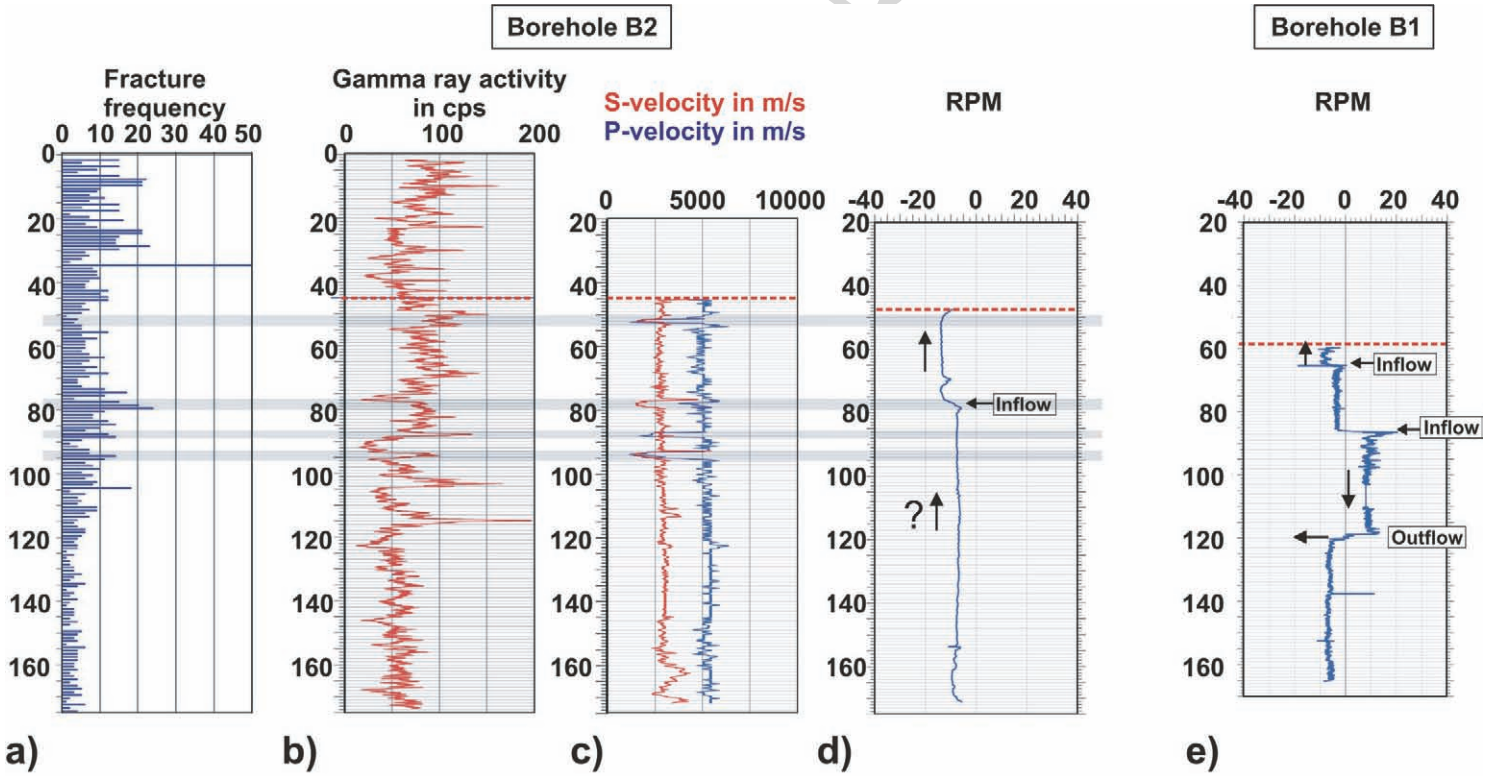

Fig.4 Heincke et al. 2009

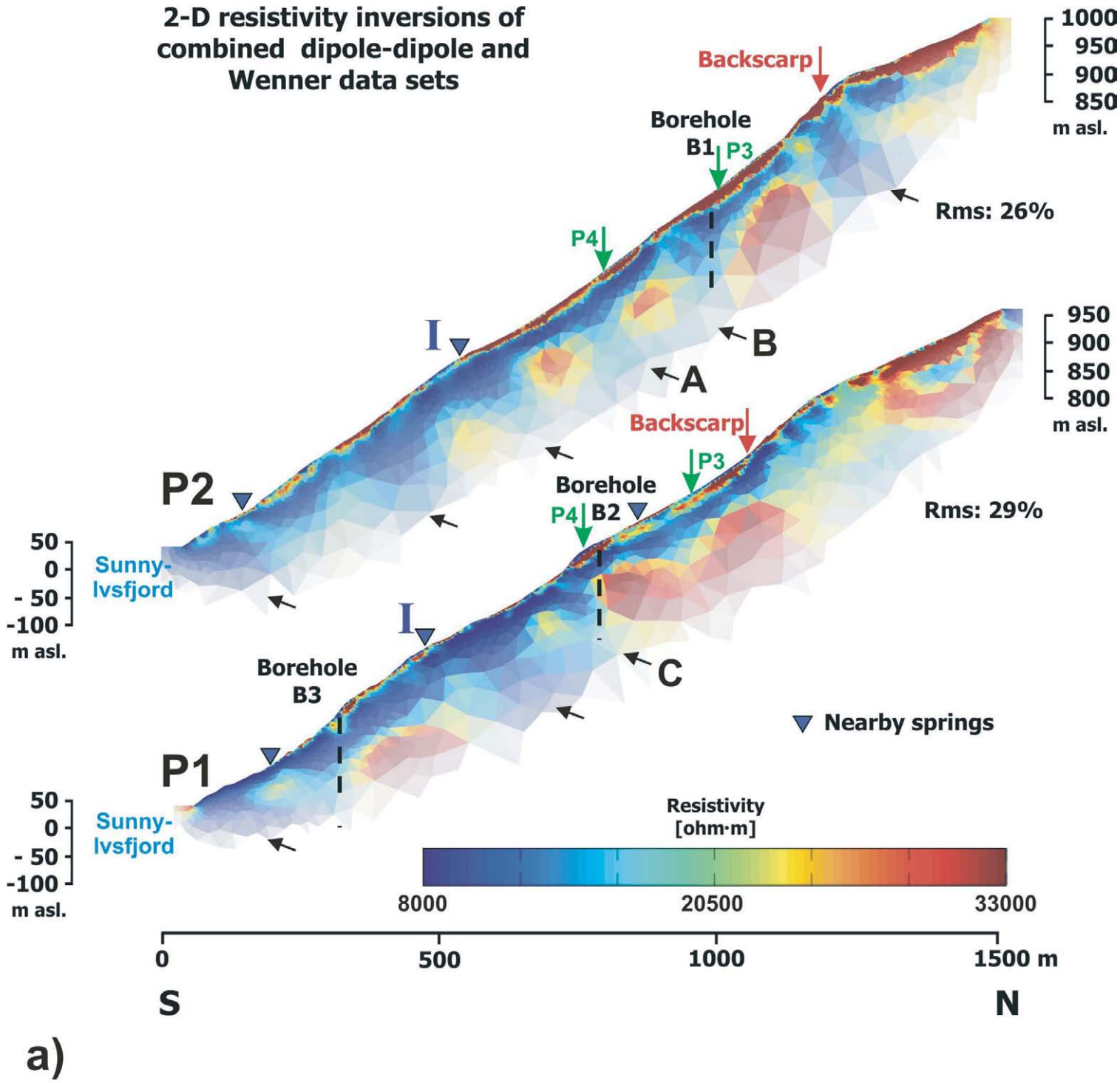

a)

Fig.5a Heincke et al. 2009

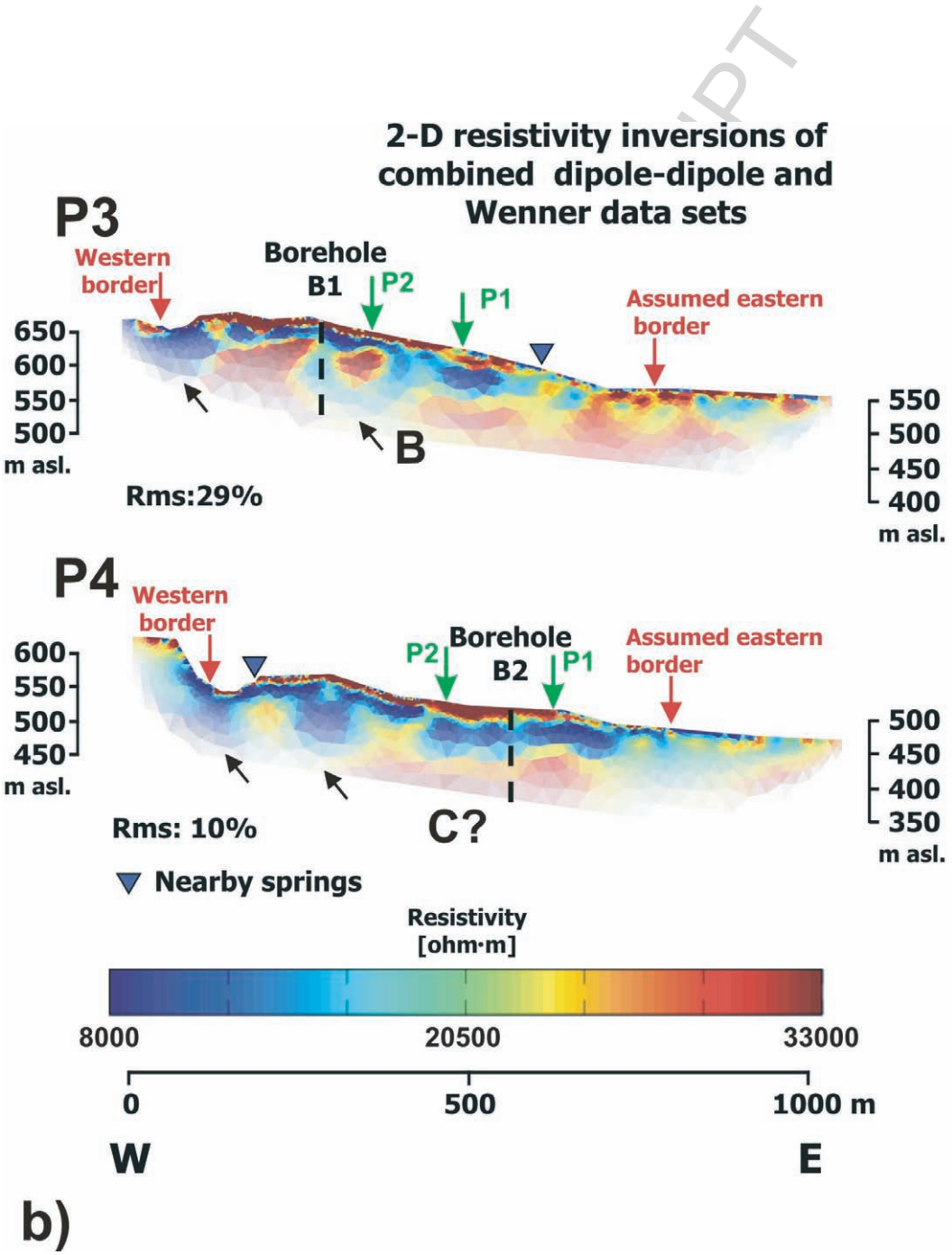

b)

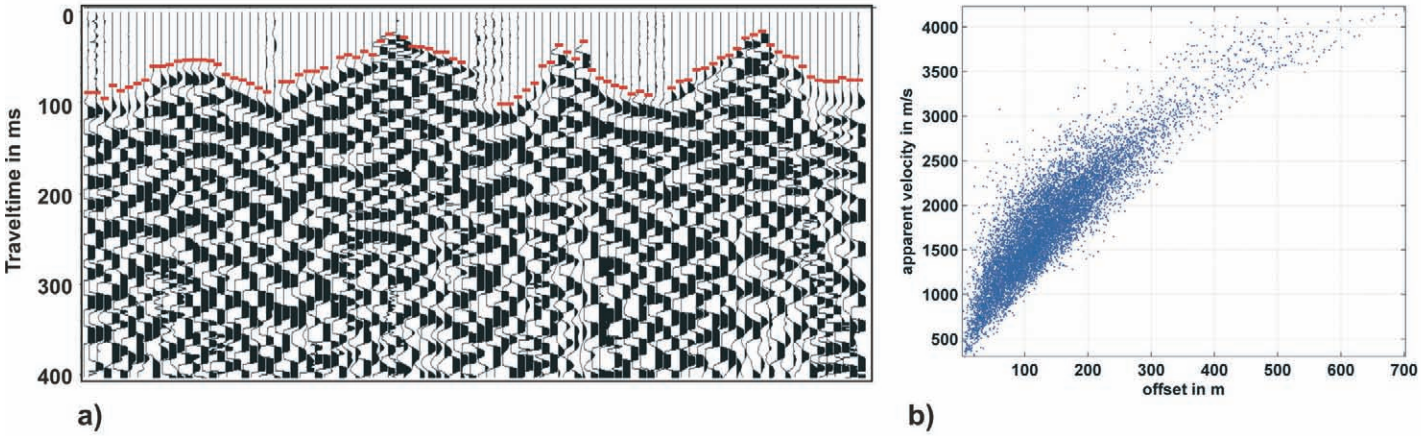

Fig.6 Heincke et al. 2009

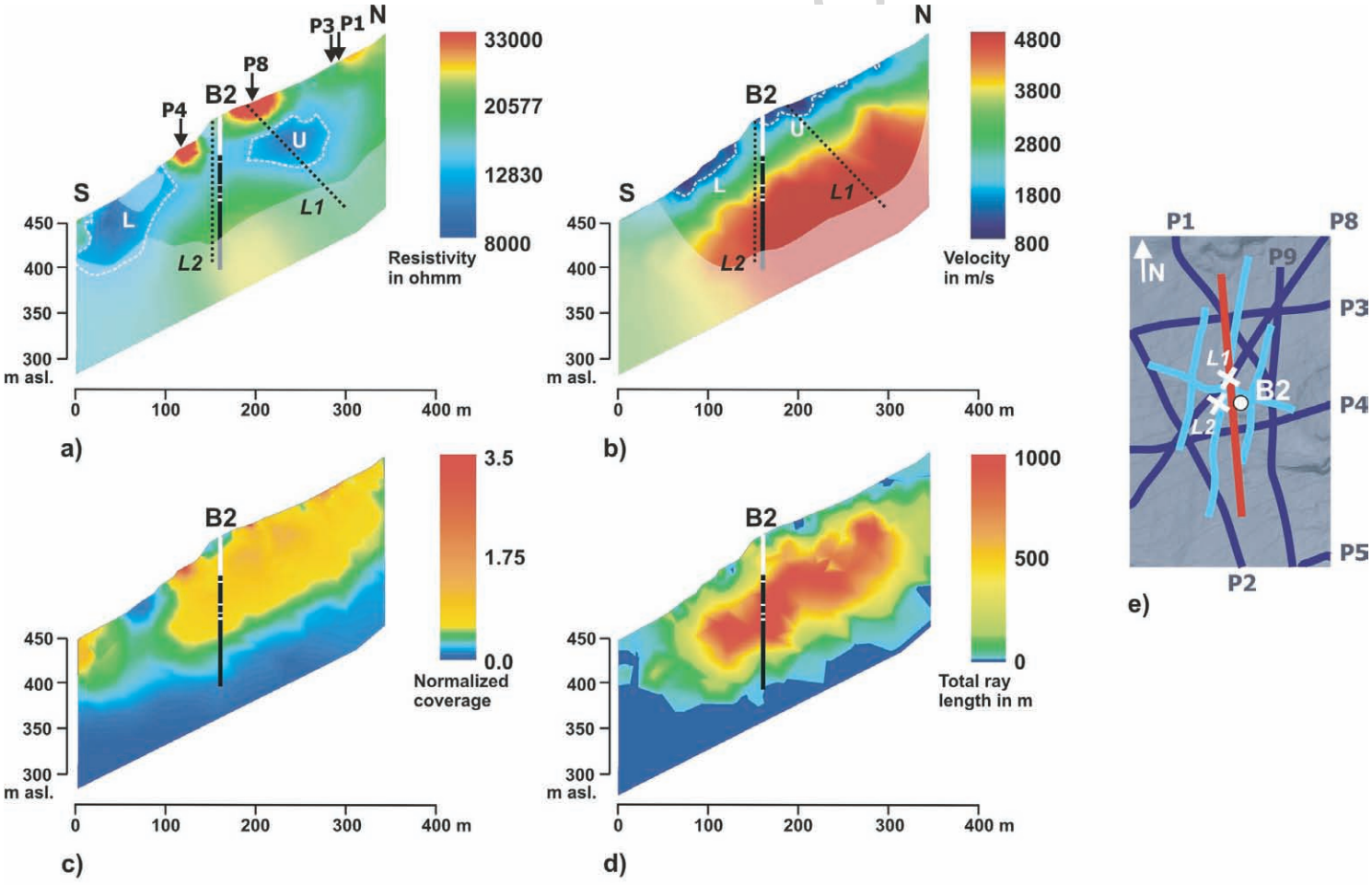

Fig.7 Heincke et al. 2009

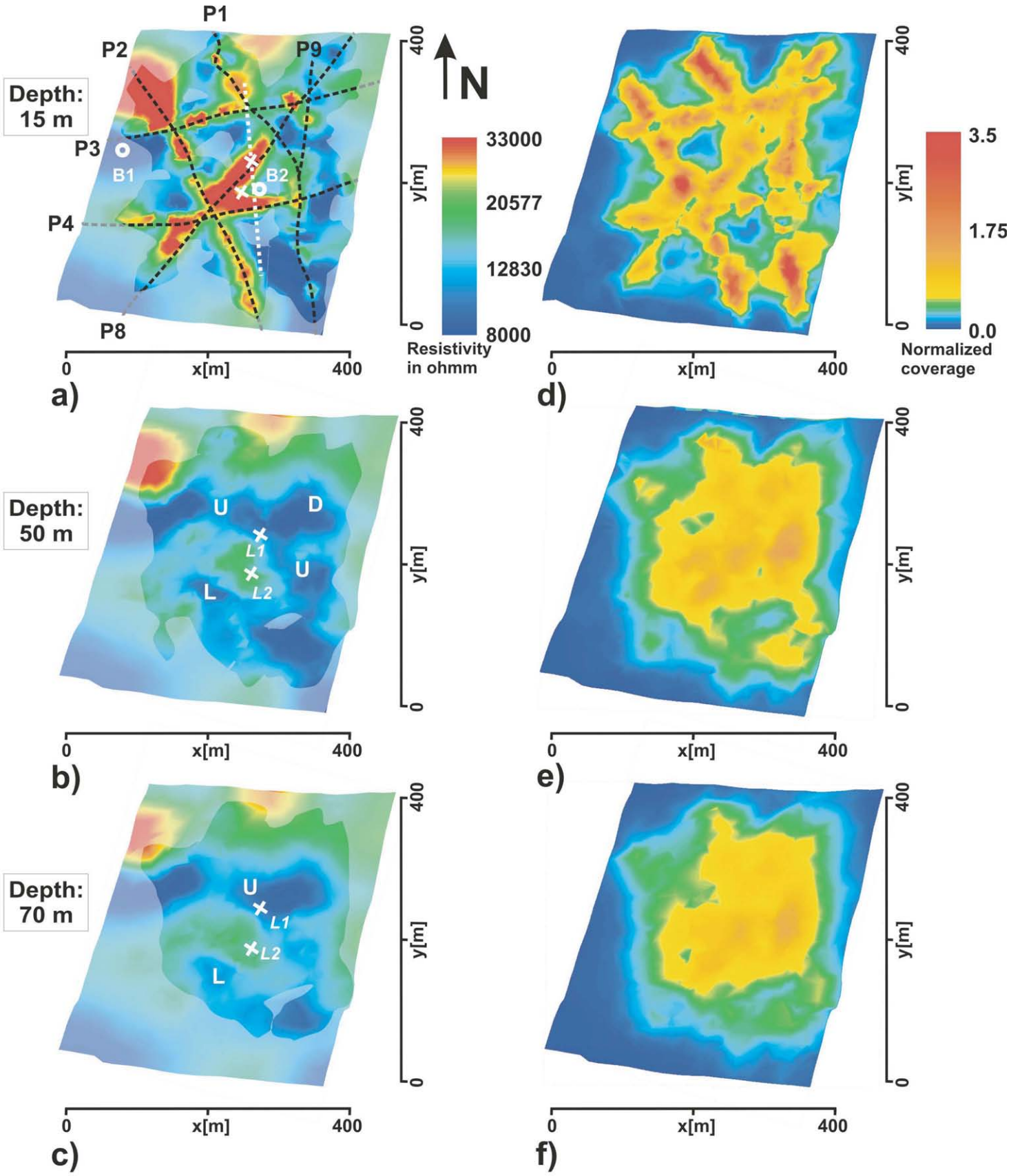

Fig.8 Heincke et al 2009

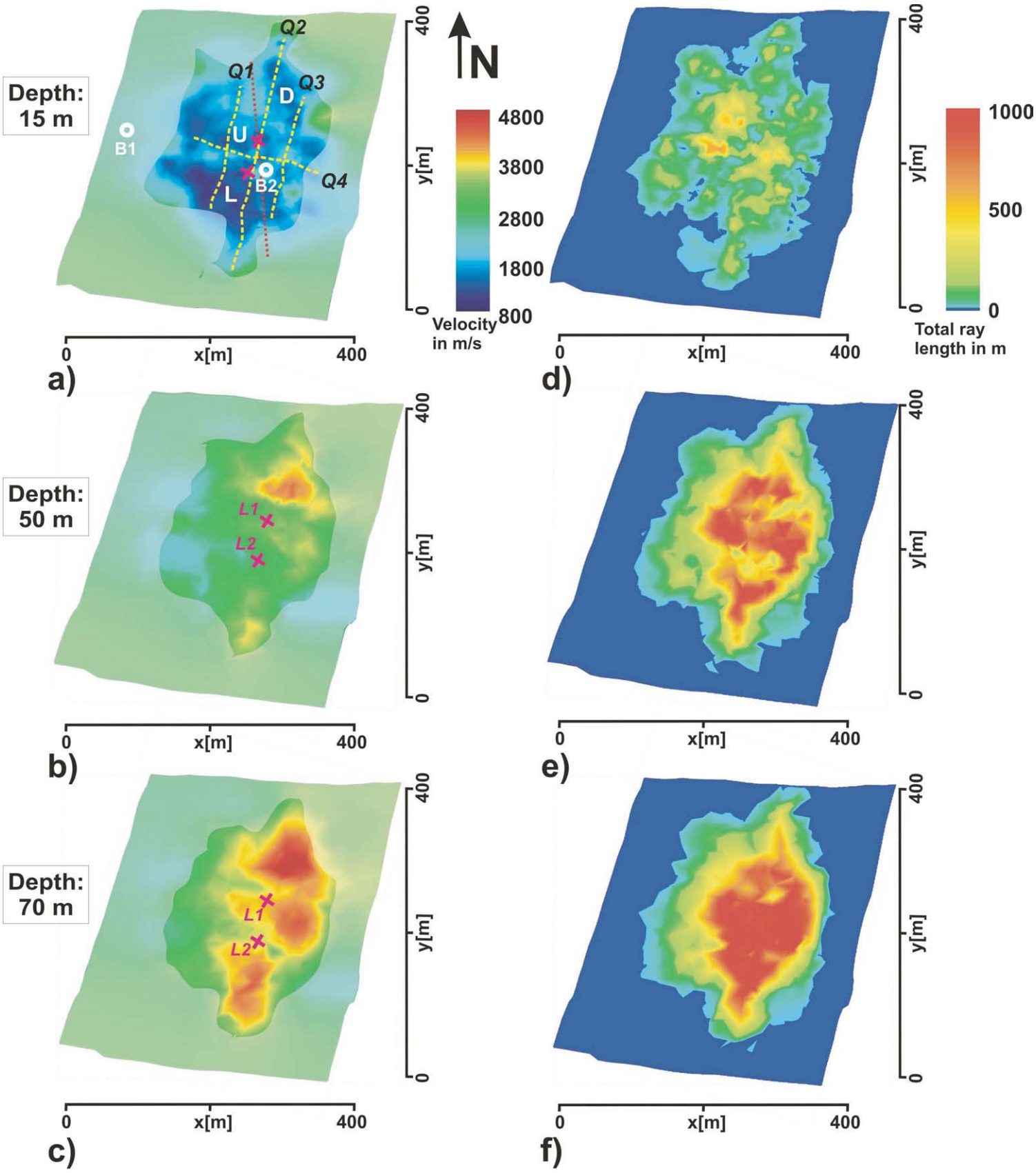

Fig.9 Heincke et al 2009

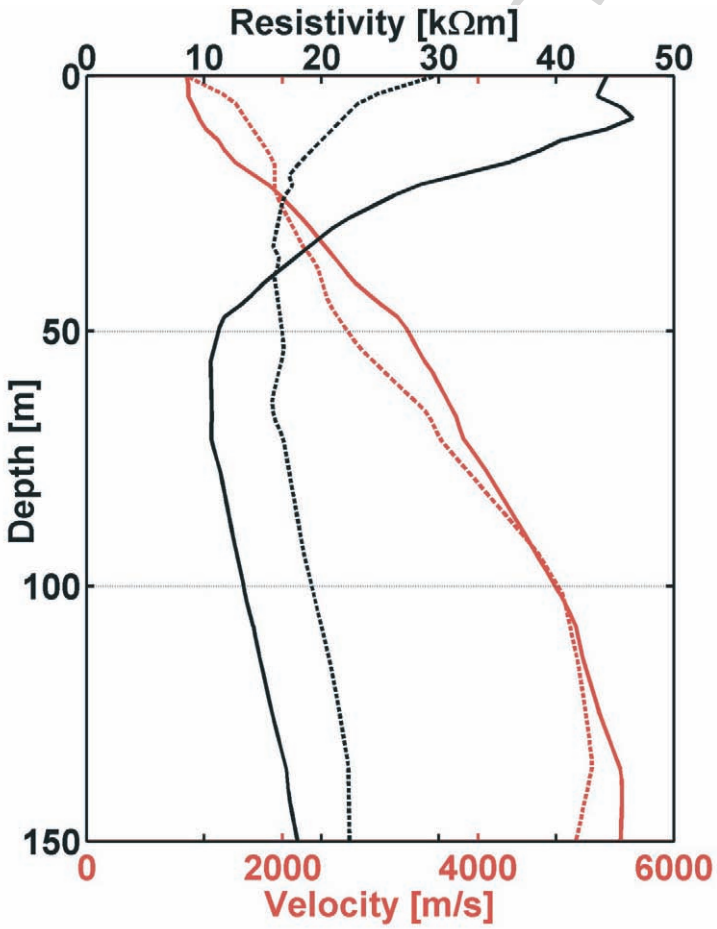

Fig.10 Heincke et al. 2009

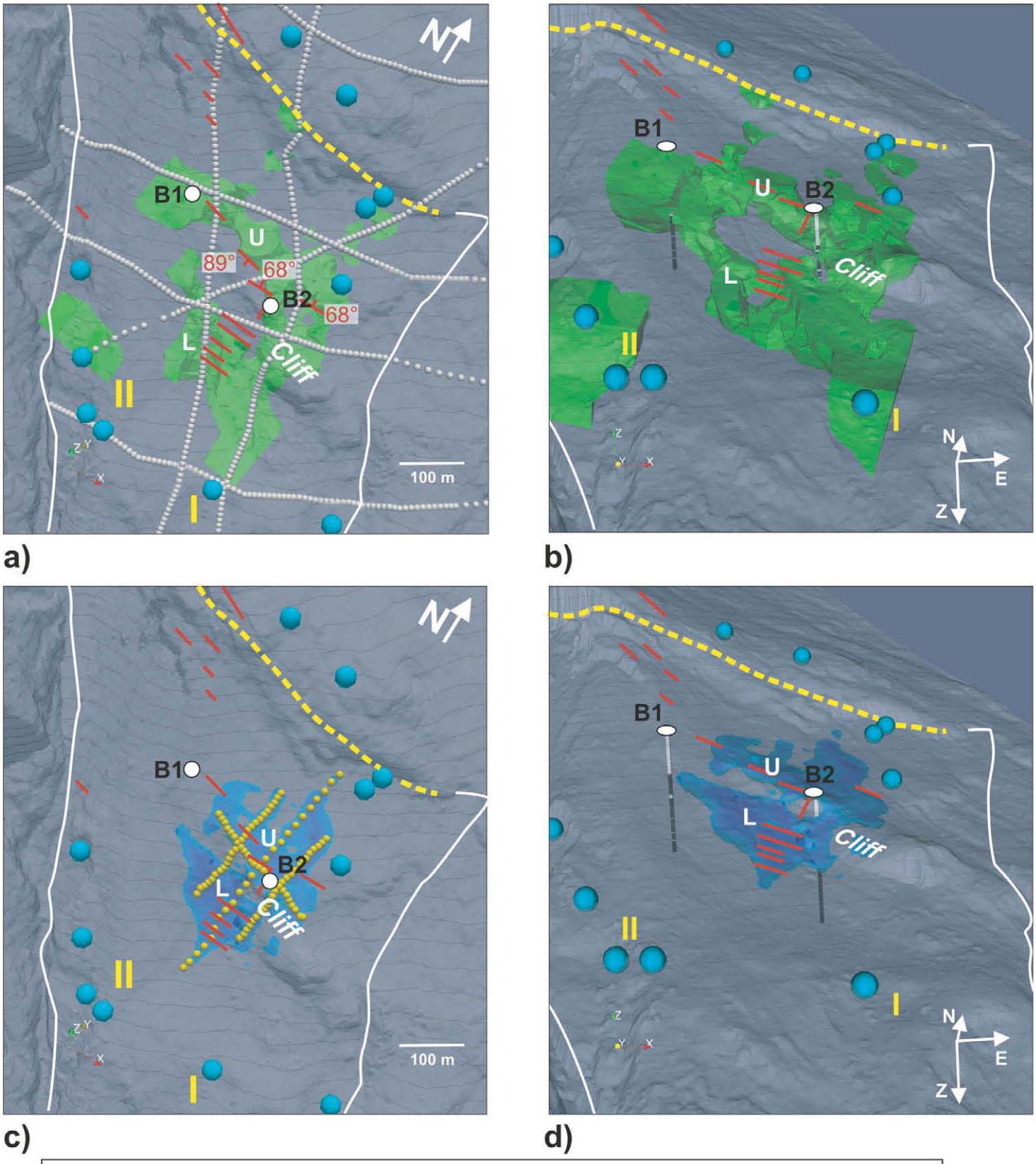

Fig.11 Heincke et al.,2009

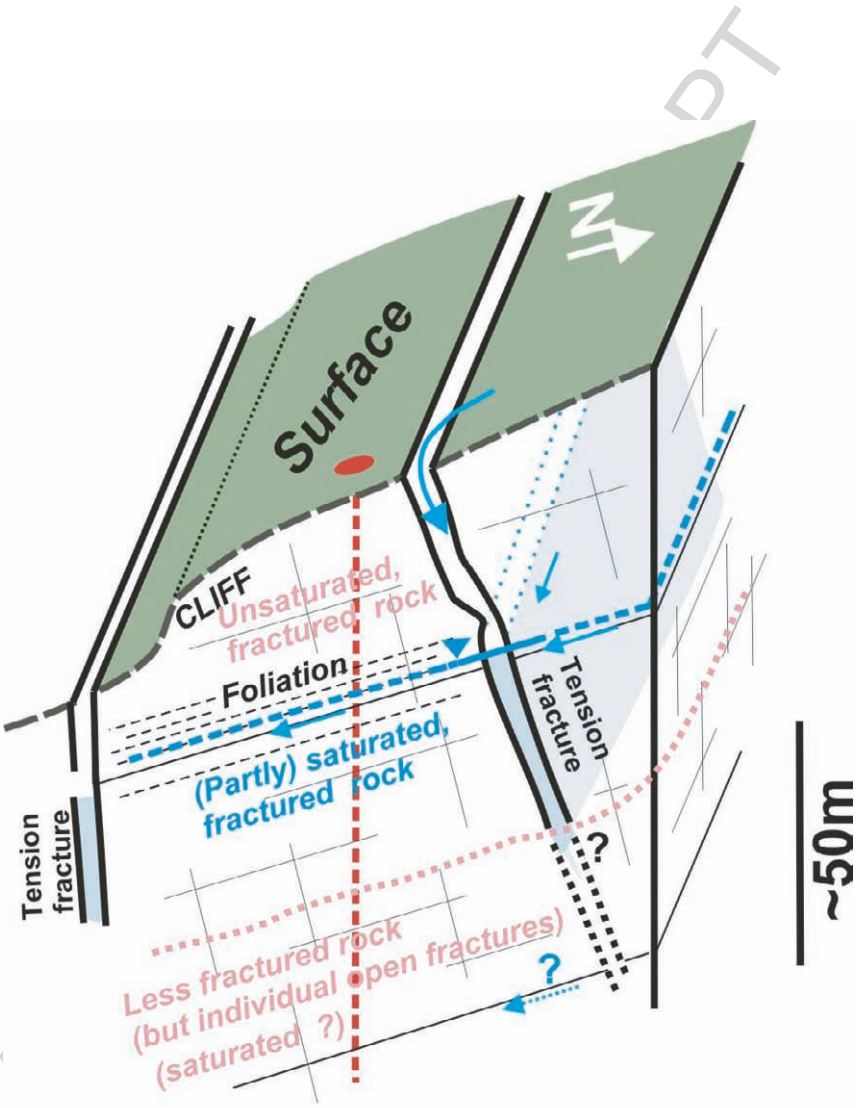

Fig.12 Heincke et al. 2009